iScience

CellPress
OPEN ACCESS

Article

Regulating oxygen vacancies in ammonium vanadate electrode materials for advanced aqueous zinc ion batteries

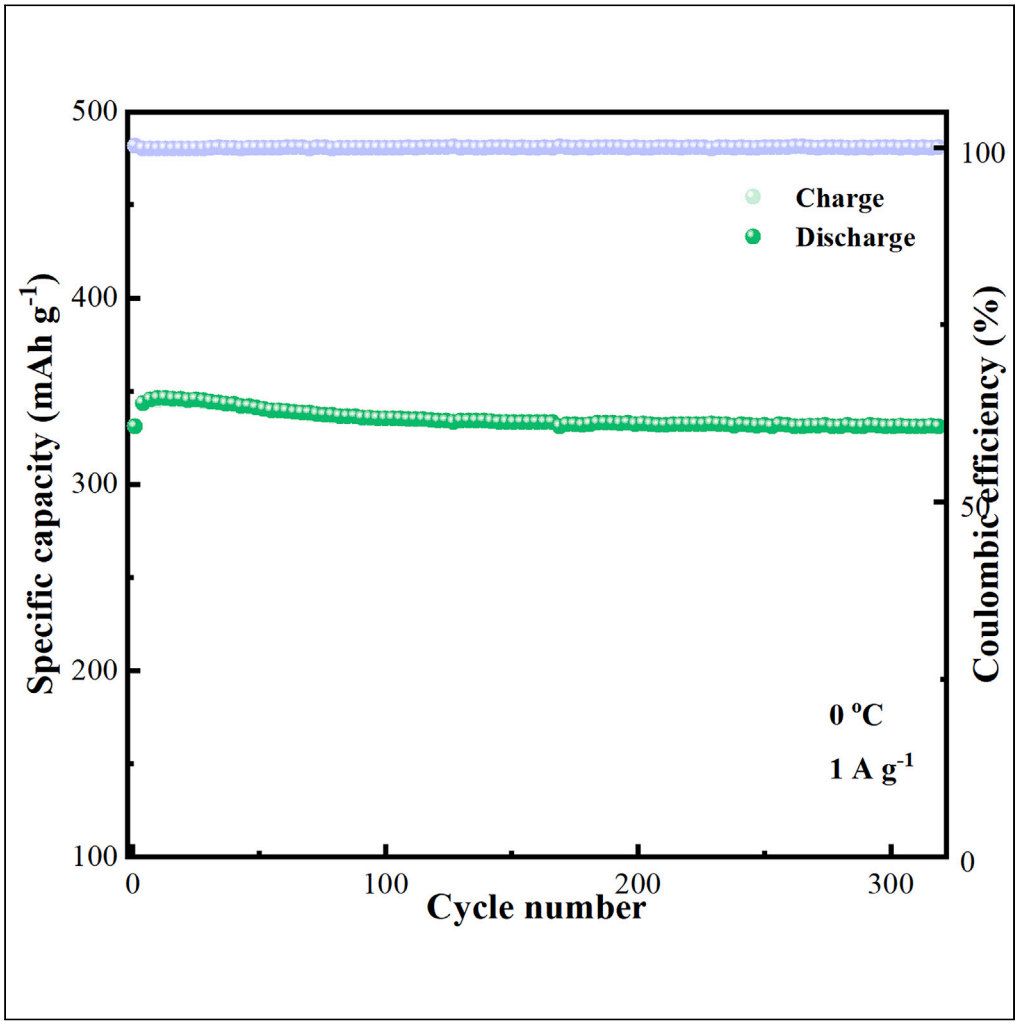

Ming Zhao, Shilong Li, Xiang Wu, Lixian Sun

wuxiang05@sut.edu.cn (X.W.)
sunlx@guet.edu.cn (L.S.)

Highlights

We have prepared oxygen vacancy-rich $NH_4V_4O_{10}$ electrode materials by a simple immersion strategy

The Zn/NHVO-40 batteries deliver a specific capacity of 452.03 mAh g^{-1} at a current density of 0.2 A g^{-1}

The cells can work within a temperature range from 0°C to 40°C

Zhao et al., iScience 27, 110926
October 18, 2024
https://doi.org/10.1016/j.isci.2024.110926

iScience

CellPress
OPEN ACCESS

Article

Regulating oxygen vacancies in ammonium vanadate electrode materials for advanced aqueous zinc ion batteries

Ming Zhao,[1] Shilong Li,[1] Xiang Wu,[1,3,*] and Lixian Sun[2,*]

SUMMARY

In the past decade, vanadates have attracted one's attention as the electrode materials for aqueous zinc ion batteries (AZIBs). Nevertheless, their structural instability and sluggish ion/electron dynamics lead to an inevitable decline in the electrochemical performance. To address these issues, we introduce oxygen vacancies into $NH_4V_4O_{10}$ nanosheets to improve the ion transport rate during the electrochemical reaction. The prepared NHVO-40 samples provide many active sites compared to $NH_4V_4O_{10}$ materials. The assembled cell delivers a capacity of 452.03 mAh g^{-1} at a current density of 0.2 A g^{-1}. It also presents a retention rate of 94.6% at 10 A g^{-1} after 4000 times cycling. In addition, they still possess an energy density of 332.5 Wh kg^{-1} at a power density of 70 W kg^{-1}.

INTRODUCTION

The increasing energy crisis has prompted one to develop some sustainable and renewable electrochemical energy storage devices.[1–4] Aqueous zinc ion batteries (AZIBs) present superior energy density, suitable redox voltage, and environmental-friendly characteristics.[5–8] They are expected to be used in domestic energy storage systems and grid regulation fields. It is very important to design the cathode materials that match well with zinc anodes.[9,10] The positive materials for AZIBs mainly include vanadium compounds,[11] manganese oxides,[12–14] Prussian blue analogs[15], and organic compounds.[16,17] Particularly, vanadium compound materials have been research focuses due to their multiple valence states, high output capacity, and open tunnels.[18,19] However, the sluggish transfer speed of Zn ions, and structural collapse limits the practical application of electrode materials.

Thus far, some modification strategies have been proposed such as coating of carbon-based materials,[20,21] ionic pre-intercalating,[22] and defect engineering.[23–25] Among them, defect engineering has been constructed to improve the electrical conductivity and suppress unnecessary phase transitions of the electrode materials. This is mainly attributed to the separation of atoms from the lattice during defect formation.[26–28] Meanwhile, the generated defects lower the reaction energy barrier between the electrolyte and electrode material and accelerate the charge transfer.

In the previous reports, Cao et al. synthesized oxygen vacancy-rich $(NH_4)_2V_{10}O_{25}\cdot 8H_2O$ nanosheets with a capacity of 160 mAh g^{-1} at a current density of 5 A g^{-1}.[29] Cui and co-workers introduced oxygen defects into $NH_4V_4O_{10}$ structure with reduced graphene oxide (rGO) decoration. The assembled Zn//$NH_4V_4O_{10}$@rGO batteries possess a capacity of 278 mAh g^{-1} at 10 A g^{-1}.[30] Wang's group synthesized V_8O_{20} nanobelts reduced by oxygen defects and surface phosphate groups. The electrode shows a capacity of 161.8 mAh g^{-1} at 10 A g^{-1} and a retention rate of 96.8% after 3000 times cycling.[31] In this work, we synthesize several $NH_4V_4O_{10}$ samples by a hydrothermal approach. The assembled Zn//NHVO-40 cells present a specific capacity of 452.03 mAh g^{-1} at 0.2 A g^{-1}. This battery still maintains a capacity of 277 mAh g^{-1} at a current density of 10 A g^{-1}. After 4000 times cycling, their specific capacity is retained at 263.9 mAh g^{-1}. Moreover, the cells present an energy density of 316.4 Wh kg^{-1} at a power density of 140 W kg^{-1}.

RESULTS AND DISCUSSION

Crystal structure and morphology

Figure 1 illustrates the synthetic schematic of the as-prepared samples. Initially, the $NH_4V_4O_{10}$ precursor is synthesized by a one-step hydrothermal route using NH_4VO_3 and $C_2H_2O_4{\cdot}2H_2O$ as raw materials. Next, the reduction treatment is used to induce oxygen vacancies into $NH_4V_4O_{10}$ products. XRD characterization is then performed to examine the crystal structure of the prepared samples. From Figure 2A, the obtained materials are indexed to the monoclinic $NH_4V_4O_{10}$ phase (PDF#31–0075). The peaks located at 9.20, 25.42, 27.50, 31.10, 34.0, and 49.78° belong to the (001), (110), (111), (400), (−311), (020) planes, respectively. The lattice parameters a = 11.71 Å, b = 3.66 Å,

[1]School of Materials Science and Engineering, Shenyang University of Technology, Shenyang 110870, P.R. China
[2]Guangxi Key Laboratory of Information Materials, Guangxi Collaborative Innovation Center of Structure and Property for New Energy Materials, Guilin University of Electronic Technology, Guilin 541004, P.R. China
[3]Lead contact
*Correspondence: wuxiang05@sut.edu.cn (X.W.), sunlx@guet.edu.cn (L.S.)
https://doi.org/10.1016/j.isci.2024.110926

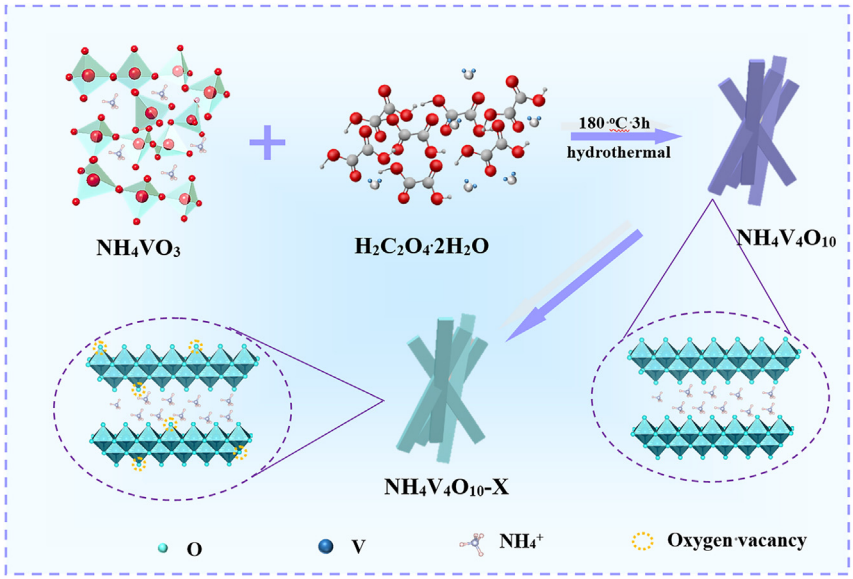

Figure 1. Synthetic route to $NH_4V_4O_{10}$ materials with rich oxygen vacancies

and c = 9.72 Å. It is seen that the intensity of the diffraction peak decreases with the treatment time increasing. This phenomenon might be attributed to the appearance of oxygen vacancies in the $NH_4V_4O_{10}$ cathodes, which is conducive to the improvement of the electrochemical performance.[32]

Subsequently, we evaluate the elemental composition and valence distribution of NHVO and NHVO-40 samples by XPS. From the full spectra, the NHVO-40 products consist of N, V, and O elements (Figure 2B). The V 2p spectra can be fitted with two spin-orbit peaks of $V2p_{1/2}$ and $V2p_{3/2}$, as described in Figure 2C. The fitting peaks at 523.1/515.7 and 524.7/517.1 eV belong to V^{4+} and V^{5+}, which confirms the existence of two mixed valence states.[33] The integral area ratio of V^{4+}/V^{5+} increases from 88% (NHVO) to 93% (NHVO-40) due to the partial conversion of V^{5+} to V^{4+}.[34] From Figure 2D, the signal peaks of O 1s spectra at 529.7, 531.8, and 533.3 eV are ascribed to V-O bond, oxygen defects, and adsorbed oxygen, respectively.[35] Meanwhile, the NHVO-40 sample possesses a larger percentage of oxygen defects compared to the pristine NHVO one. Furthermore, electron paramagnetic resonance (EPR) is also utilized to prove the presence of oxygen vacancies in the samples. Figure 2E presents a sharp and strongly symmetric peak at g = 2.004, which is a typical signal for oxygen defects.[34] The NHVO-40 sample demonstrates a higher intensity than the NHVO electrode material, indicating its sufficient oxygen vacancies. It is consistent with the above XPS results. From Figure 2F, NHVO-40 materials possess a larger specific surface area (34.14 m^2/g) and pore size (0.331 cm^3/g) than NHVO samples (27.10 m^2/g, 0.251 cm^3/g). It demonstrates that oxygen vacancies benefit by increasing the active sites and facilitating the transport of Zn ions.

SEM is then utilized to observe the morphology of the obtained samples. From Figure 3A, the NHVO precursor presents a typical nanobelt structure with a smooth surface. It is found that all samples possess similar shapes, as shown in Figures 3B–3D. Figure 3E shows low magnification TEM image of the NHVO-40 sample with a rough surface. The corresponding HRTEM image (Figure 3F) presents a lattice fringe of 0.201 nm, and it belongs to the (−312) crystal plane of the $NH_4V_4O_{10}$ sample. Meanwhile, there are some lattice disorders associated with defects.[36] The elemental mappings (Figure 3G) suggest the uniform distribution of N, V, and O elements on the surface of the samples.

Electrochemical performance and reaction kinetics of Zn//NHVO-X cell

After that, we assemble some CR2032 cells to evaluate the practical application of the products in 3 M $Zn(CF_3SO_3)_2$ electrolytes. Figure 4A presents the CV curves of the NHVO-40 electrode at 0.2 mV s^{-1}. There is a similar shape of the CV curves in the first four cycles, demonstrating their high reversibility in the reaction process. As shown in Figure 4B, NHVO-40 samples deliver a specific capacity of 452 mA h g^{-1} at 0.2 A g^{-1} and maintain 388 mA h g^{-1} after 100 cycles. It retains 85.8% of its initial capacity, which is superior to other cathodes (NHVO:78.2%, NHVO-30:82.4%, NHVO-50:70.7%). Several plateaus of the GCD curves (Figure 4C) are coincident with the peaks of the CV ones. At a current density of 0.1 A g^{-1}, the initial discharge capacity is 483.9 mAh g^{-1} and decreases slightly in the next few cycles. The capacity at different current densities also is an important factor in assessing the performance of batteries. The rate performances of Zn//NHVO-30/40/50 cells are then investigated at current densities from 0.1 to 10 A g^{-1} (Figure 4D). The corresponding discharge specific capacities are 475.6, 452.0, 437.7,428.6, 422.6, 419.5, 398.6, 383.9, 355.5, and 303.4 mAh g^{-1}, respectively. As the current density returns to 0.2 A g^{-1}, its capacity remains 450.4 mAh g^{-1}, which is 99.6% of the initial state. It is noticed that the capacity of the NHVO-40 cathode material is obviously higher than those of the others at 10 A g^{-1}. The structural stability of the samples is also explored by long cycling tests at the same current densities. It can be seen that the initial specific capacity of the NHVO-40 electrode is 278.12 mAh g^{-1}, which is excellent than those of the other three materials

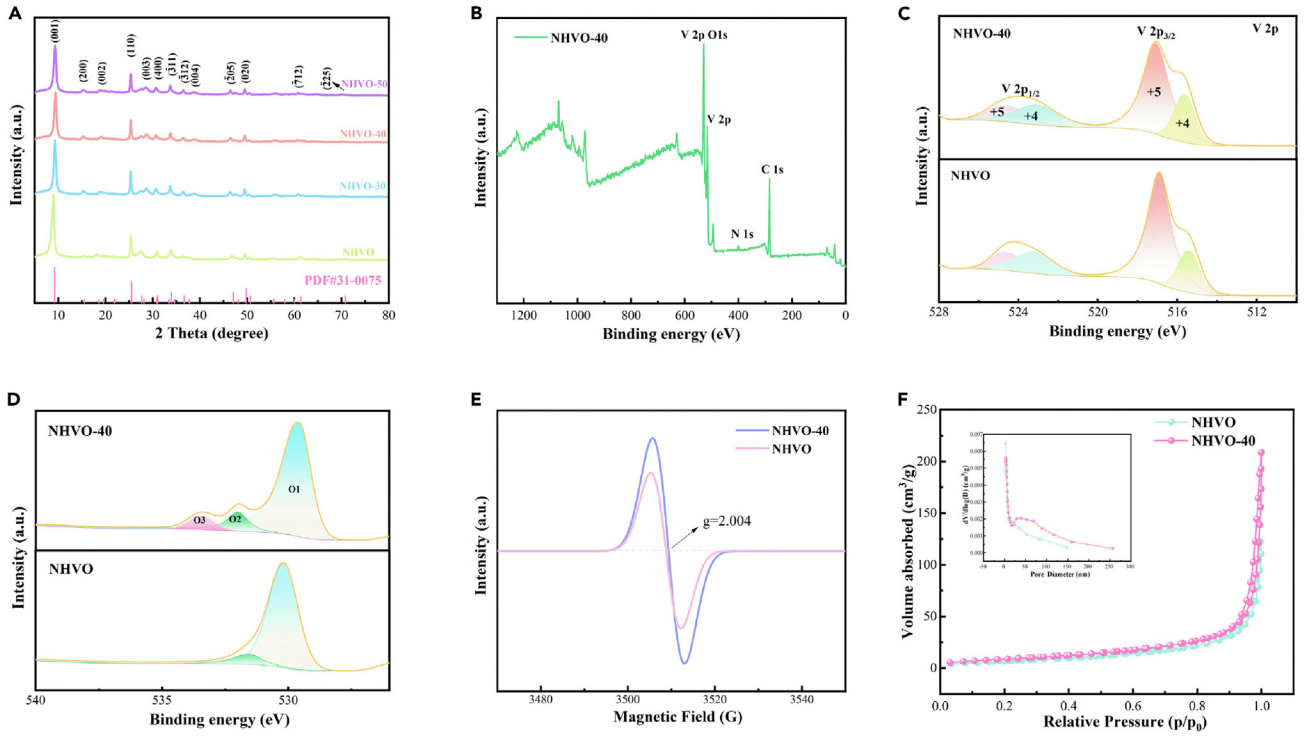

Figure 2. Structural characterization

(A) XRD patterns of the $NH_4V_4O_{10}$ samples with different treatment times.

(B) XPS survey spectra of NHVO-40 materials.

(C) V 2p.

(D) O 1s.

(E) EPR spectroscopy of the NHVO and NHVO-40 cathodes.

(F) N_2 adsorption-desorption isotherms and inset the pore size distribution curves.

(Figure 4E). Meanwhile, it still keeps 263.9 mAh g^{-1} and almost 100% Coulombic efficiency after 4000 times cycling. Figure 4F shows the corresponding GCD curves at current density varying from 0.1 to 10 A g^{-1}. And it indicates a gradual decrease in capacity as the current density increases. The shape of these curves remains constant after tens of cycles, indicating a favorable stability of the electrode materials. Table 1 lists the specific capacity of several cathode materials,[37–42] demonstrating the superior electrochemical performance of the as-prepared samples. We also study the electrochemical performance at different work temperatures. From Figure 4G, the Zn//NHVO-40 batteries deliver a specific capacity of 328.48, 388.25, 442.71, and 497.47 mAh g^{-1} when the temperature varies from 0 to 40°C. The assembled cells achieve a specific capacity of 345.38 mAh g^{-1} at 0°C (1 A g^{-1}). Meanwhile, it keeps a capacity of 331.11 mAh g^{-1} and almost 100% coulombic efficiency after 320 times cycling (Figure 4H).

Afterward, the CV curves are utilized again to evaluate the electrochemical kinetic behavior. With the sweep speed increasing, the integration area enlarges and maintains a similar shape, showing the excellent reversibility of the redox reaction. As seen from Figure 5A, there are three pairs of redox peaks located at 1.36/0.97, 1.09/0.80, and 0.65/0.41 eV, respectively. It suggests that the obtained samples undergo a multi-step redox reaction during Zn^{2+} insertion/de-insertion. In literature, the reaction control behavior can be determined by the relationship between the peak current (i) and the scan rate (v) based on the following equation:

$$i = av^b \quad \text{(Equation 1)}$$

Figure 5B shows that the fitted b values are 0.98, 1.06, 0.84, 1.01, 0.9, and 0.77, respectively. This result implies that the reaction is dominated by the surface capacitive behavior. Subsequently, we calculate the capacity contribution through Equation 2.

$$i(V) = k_1v + k_2v^{1/2} \quad \text{(Equation 2)}$$

Thereinto, k_1v denotes surface-controlled contribution, while $k_2v^{1/2}$ is the diffusion controlled one. The capacitive contribution is 91.6% at a sweep speed of 0.2 mV s^{-1}. And then it can reach up to 97.3% at the scanning rate of 1 mV s^{-1} (Figure 5C).

Then we investigate the diffusion coefficient of zinc ions (D_{Zn}^{2+}) during cycling by using the galvanostatic intermittent titration technique (GITT). Figure 5D indicates that the D_{Zn}^{2+} of the NHVO-40 cathode is between 10^{-6}-10^{-8}, revealing the fast migration ability of Zn^{2+}. From the

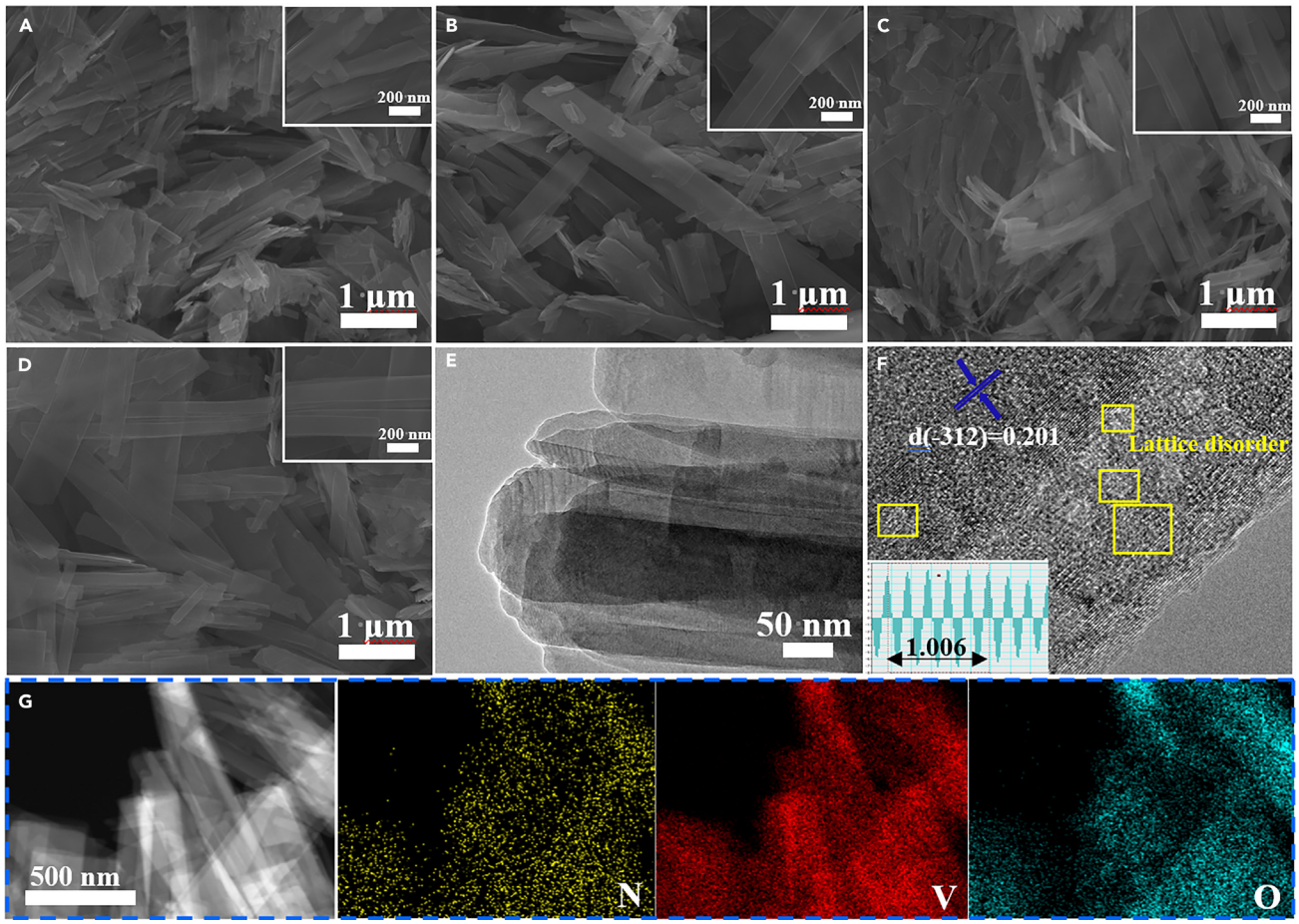

Figure 3. SEM images

(A) NHVO.
(B) NHVO-30.
(C) NHVO-40.
(D) NHVO-50.
(E) TEM image of NHVO-40 samples.
(F) HRTEM image of NHVO-40 electrodes.
(G) element mapping images.

EIS spectra in Figure 5E, the four curves of the prepared samples are composed of a semicircle in the high frequency region and a straight line in the low one. The former represents the charge transfer resistance (R_{ct}) between the electrode and electrolyte, and the latter denotes the Warburg impedance (Z_w) of Zn^{2+} diffusion. The NHVO-40 material shows a lower charge transfer resistance (54.32 Ω) than the other electrodes. Power density and energy density are important factors of zinc ion batteries. It can be calculated via Equations 3 and 4 later in discussion:

$$E = QU/2m \quad \text{(Equation 3)}$$

$$P = iU/2m \quad \text{(Equation 4)}$$

where Q, U, I, and m refer to the discharge capacity, operating voltage, discharge current, and the mass of active substances, respectively. The obtained sample delivers an energy density of 332.5 Wh kg^{-1}at a power density of 70 W kg^{-1}. When it is increased to 3500 W kg^{-1}, the corresponding energy density is 249 Wh kg^{-1}. It is superior to some reported materials, such as $NH_4V_4O_{10-x}$@rGO, C_3N_4-$NH_4V_4O_{10}$ and K/PANI-V_2O_5 electrodes (Figure 5F).[43–48]

Storage mechanism of NHVO-40 samples

Finally, the energy storage mechanism of NHVO-40 cathodes is further explored via *ex situ* XRD during the charging/discharging. As shown in Figure 6A, the (−311) crystal plane gradually shifts to a low angle in the discharge state. The characteristic peak then returns to its initial state

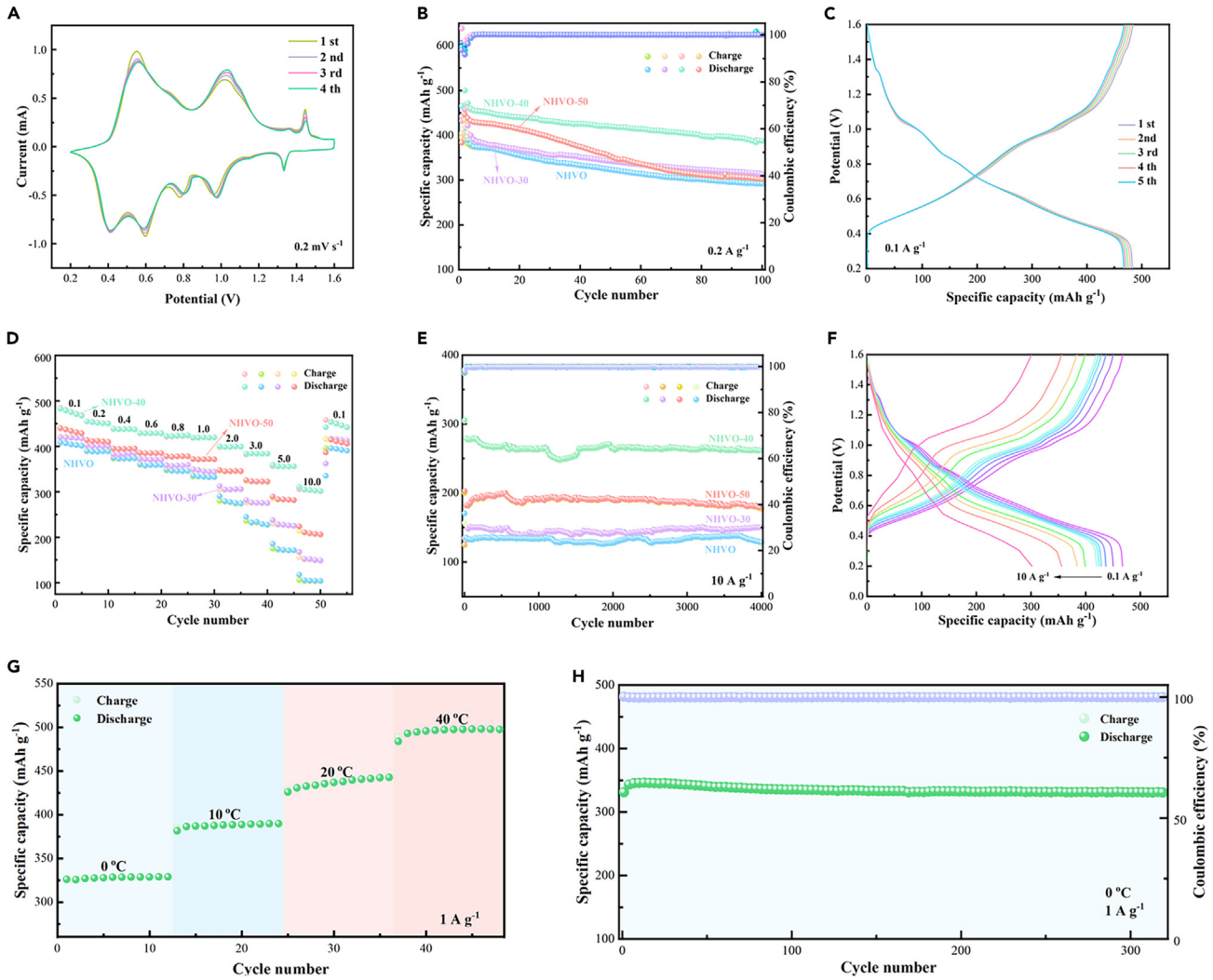

Figure 4. Electrochemical performance

(A) CV curves in the first 4 cycles at 0.2 mV s^{-1}.

(B) cycle curves at 0.2 A g^{-1}.

(C) GCD curves at 0.1 A g^{-1}.

(D) rate performance.

(E) cycling stability at 10 A g^{-1}.

(F) GCD curves at different current densities.

(G) cycling performance at various temperatures.

(H) cycling stability at 0°C.

when charged to 1.6 V. The variation of crystal spacing during the reaction is attributed to the embedding and de-embedding of Zn^{2+} in the host material.[49] It proves the reversible structural evolution of the cathode. Some additional peaks are also observed at 12.2° and 17.08°, which can match well with $Zn_3(OH)_2V_2O_7{\cdot}2H_2O$ phase (JCPDS No. 50–0570). The formation of the by-product is ascribed to the participation of OH^- in the reaction, which may come from the decomposition of the aqueous electrolyte.[50] Excess H^+ also participates in the electrochemical reaction to maintain the charge balance of the system. Thus, the assembled cells follow H^+ and Zn^{2+} co-(de)insertion energy storage mechanism.

The *ex situ* XPS are carried out to further reveal the change in the surface composition and the valence state of the NHVO-40 electrode. In Figure 6B, the peak intensity of O3 is enhanced initially and then reduced during the discharged and charged states. This manifests that the $Zn_3(OH)_2V_2O_7{\cdot}2H_2O$ phases are formed or some adsorbed H_2O are participated in the reaction process. From the V 2p spectra (Figure 6C), the peaks at 515.6/523.5, and 517.5/524.9 eV are assigned to V^{4+} and V^{5+}, respectively. In the discharge process, the slight increase of V^{4+} content is accompanied by a decrease of V^{5+}, which is due to the embedding of Zn^{2+}. The high-resolution of Zn 2p spectra is demonstrated in Figure 6D. There are no obvious diffraction peaks to be found in the pristine state. When the cell is discharged to 0.2 V, two distinct peaks appear

Table 1. The electrochemical performances of the NHVO-40 electrode material

Materials	Morphology	Current density (A g^{-1})	Discharge capacity (mAh g^{-1})	Electrolyte	Reference
MnVO-PANI	microspheres	0.1	462	3 M $Zn(CF_3SO_3)_2$	Zhang et al.[33]
$K_{0.09}Mg_{0.03}V_2O_5 \cdot nH_2O$	microspheres	0.1	423	3 M $Zn(CF_3SO_3)_2$	Wang et al.[34]
$(NH_4)_2V_{10}O_{25} \cdot 8H_2O$	belts	0.1	417	3 M $Zn(CF_3SO_3)_2$	Zhuang et al.[35]
$(NH_4)_2V_3O_8$/C	nanoparticles	0.1	356	3 M $Zn(CF_3SO_3)_2$	Li et al.[36]
$NH_4V_4O_{10}$	nanocables	0.1	430	2 M $ZnSO_4$ + 3 M $Zn(CF_3SO_3)_2$	Zhang et al.[37]
$(NH_4)_2V_6O_{16} \cdot 1.5H_2O$	nanowires	0.1	385	3 M $Zn(CF_3SO_3)_2$	Feng et al.[38]
NHVO-40	nanosheets	0.1	475.6	3 M $Zn(CF_3SO_3)_2$	This work

at 1022 eV and 1045.1 eV. They are ascribed to the $Zn2p_{1/2}$ and $Zn2p_{3/2}$ orbitals, indicating the successful intercalation of Zn^{2+} into the host structure. In contrast, the intensity of the peak reduces in the fully charged state, which still shows a small portion of the Zn signal existing. This is due to the irreversible removal of some Zn^{2+}. As shown in Figures 6E and 6G, the NHVO-40 sample still retains the microscopic morphology of the nanobelts during different reaction processes. Subsequently, HRTEM is employed to study the variation of lattice spacing. Figure 6F indicates the lattice distance of 0.329 nm, which matches well with the (420) plane of the $NH_4V_4O_{10}$ phase. And the lattice fringe then shrinks to 0.326 nm when charged to 1.6 V (Figure 6H).

Conclusions

In summary, we have prepared oxygen vacancy-rich $NH_4V_4O_{10}$ electrode materials by a simple immersion strategy. The Zn/NHVO-40 cells possess favorable specific capacity, long cycle life, and large specific surface area. Meanwhile, the assembled system also presents a high

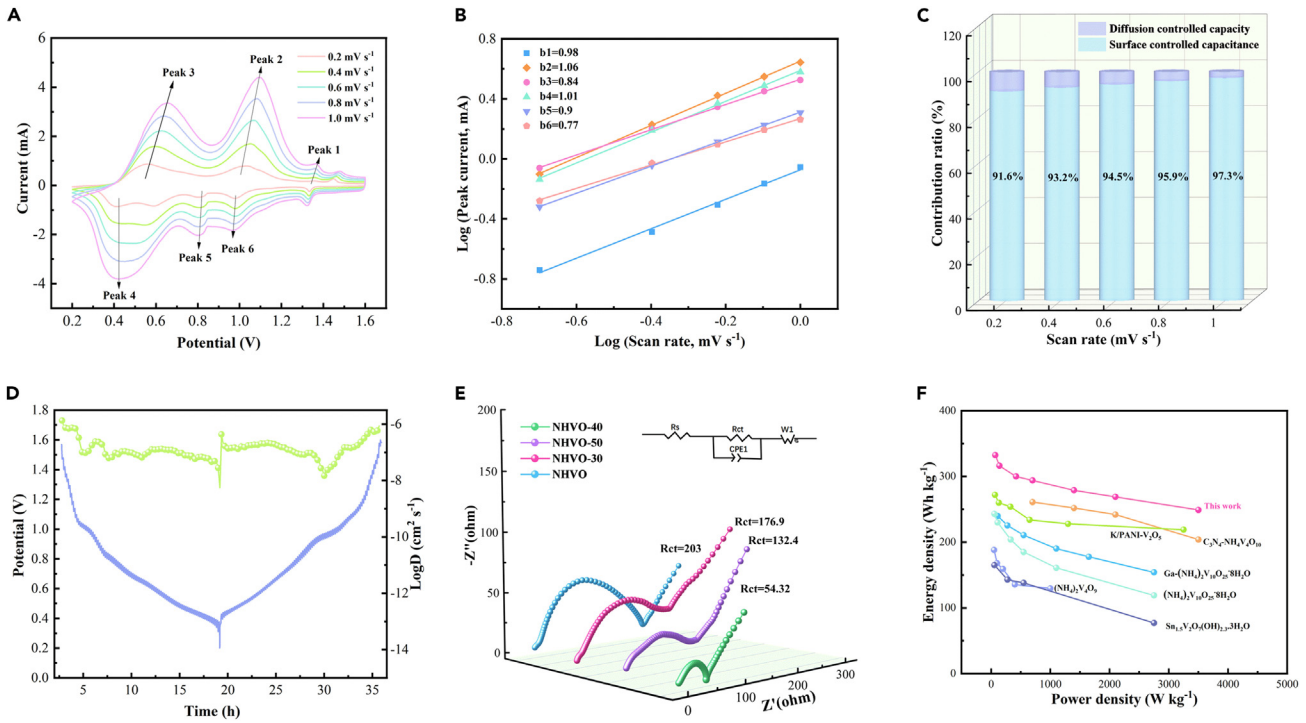

Figure 5. Electrochemical reaction kinetics of the electrodes

(A) CV curves at different scan rates.

(B) fitting plots of log(i) and log(v).

(C) the capacitive contribution ratios of NHVO-40 cathodes.

(D) GITT curves.

(E) Nyquist plots.

(F) Ragone plot.

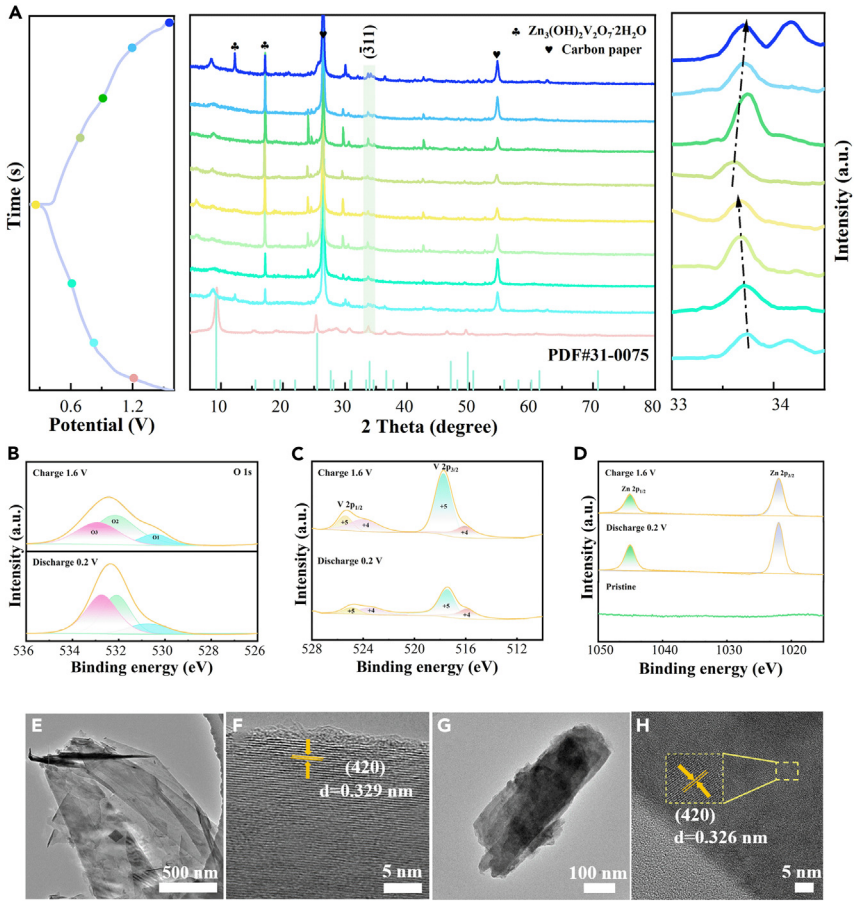

Figure 6. Energy storage mechanism of the NHVO-40 electrodes

(A) ex situ XRD patterns at different states.

(B–D) XPS spectra of O, V, Zn elements.

(E and F) discharging at 0.2 V.

(G and H) charging at 1.6 V.

energy density. Thus, the introduction of the appropriate amount of oxygen defects in $NH_4V_4O_{10}$ samples not only increases the active sites, and accelerates the electron transfer rate, but also improves the electrochemical activity. This work proposes an effective vacancy modulation strategy for the construction of high-performance zinc ion batteries. And the prepared cathode material presents potential applications in next generation energy storage systems.

RESOURCE AVAILABILITY

Lead contact

Further information and requests for resources and materials should be directed to and will be fulfilled by the lead contact, Prof. Xiang Wu (wuxiang05@sut.edu.cn).

Materials availability

The study did not generate new unique materials. The readers can buy the chemicals to remake the materials as mentioned in the text.

Data and code availability

- Data: All data reported in this article will be shared by the lead contact upon request.
- Code: This article does not report the original code.
- Any additional information required to reanalyze the data reported in this article is available from the lead contact upon request.
- All data supporting the findings of this study are available within the article and from the corresponding authors upon reasonable request.

ACKNOWLEDGMENTS

This project is supported by the Natural Science Foundation (No. 52172218) and Guangxi Key Laboratory of Information Materials & Guangxi Collaborative Innovation Center of Structure and Property for New Energy Materials (No. 231026-K).

AUTHOR CONTRIBUTIONS

Zhao, M., Methodology, conceptualization, software, data curation, and writing-original draft preparation. Li, S.L., Visualization and software. Wu X. and Sun Lixian, Supervision and writing-reviewing and editing.

DECLARATION OF INTERESTS

The authors declare no conflicts of interest.

STAR★METHODS

Detailed methods are provided in the online version of this paper and include the following:

- KEY RESOURCES TABLE
- EXPERIMENTAL MODEL AND STUDY PARTICIPANT DETAILS
- METHOD DETAILS
  - Preparation of $NH_4V_4O_{10}$ nanosheets
  - Structural characterization
  - Electrochemical characterization
- QUANTIFICATION AND STATISTICAL ANALYSIS
- ADDITIONAL RESOURCES

Received: July 13, 2024
Revised: August 21, 2024
Accepted: September 9, 2024
Published: September 11, 2024

REFERENCES

1. Wang, K., Pei, P., Zuo, Y., Wei, M., Wang, H., Zhang, P., Chen, Z., and Shang, N. (2022). Magnetic zinc-air batteries for storing wind and solar energy. iScience *25*, 103837.
2. Jiang, H., Zhang, Y., Waqar, M., Yang, J., Liu, Y., Sun, J., Feng, Z., Sun, J., Pan, Z., Meng, C., and Wang, J. (2023). Anomalous Zn^{2+} storage behavior in dual-ion-in-sequence reconstructed vanadium oxides. Adv. Funct. Mater. *33*, 2213127.
3. Liu, Y., and Wu, X. (2024). Metal-organic framework assisted design of $ZnVO_x$ cathode for aqueous zinc batteries at extreme work condition. Nano Energy *127*, 109809.
4. Wu, M., Zhang, Y., Xu, L., Yang, C., Hong, M., Cui, M., Clifford, B.C., He, S., Jing, S., Yao, Y., and Hu, L. (2022). A sustainable chitosan-zinc electrolyte for high-rate zinc-metal batteries. Matter *5*, 3402–3416.
5. Grignon, E., Battaglia, A.M., Schon, T.B., and Seferos, D.S. (2022). Aqueous zinc batteries: design principles toward organic cathodes for grid applications. iScience *25*, 104204.
6. Liu, Y., Liu, Y., Wu, X., and Cho, Y.R. (2023). General carbon modification avenue to construct highly stable V_2O_5 electrodes for aqueous Zinc-ion batteries. ACS Sustain. Chem. Eng. *11*, 13298–13305.
7. Zheng, Z., Shi, W., Zhou, X., Zhang, X., Guo, W., Shi, X., Xiong, Y., and Zhu, Y. (2023). Agar-based hydrogel polymer electrolyte for highperformance zinc-ion batteries at all climatic temperatures. iScience *26*, 106437.
8. Feng, Z., Zhang, Y., Gao, Z., Hu, D., Jiang, H., Hu, T., Meng, C., and Zhang, Y. (2024). Construction interlayer structure of hydrated vanadium oxides with tunable P-band center of oxygen towards enhanced aqueous Zn-ion batteries. Advanced Powder Materials *3*, 100167.
9. Yang, J.L., Yang, P., Xiao, T., and Fan, H.J. (2024). Designing single-ion conductive electrolytes for aqueous zinc batteries. Matter *7*, 1928–1949.
10. Xu, Z., Li, Y., Li, G., Zhang, H., and Wang, X. (2023). Reversible zinc powder anode via crystal facet engineering. Matter *6*, 3075–3086.
11. Liu, Y., and Wu, X. (2023). High durable aqueous zinc ion batteries by synergistic effect of V_6O_{13}/VO_2 electrode materials. J. Energy Chem. *87*, 334–341.
12. Li, S., Zhao, M., Zhang, D., and Wu, X. (2023). High-capacity aqueous Zn/MnO_2 batteries: a clue of K ion preintercalation. Cryst. Growth Des. *23*, 8156–8162.
13. Liu, Y., and Wu, X. (2022). Strategies for constructing manganese-based oxide electrode materials for aqueous rechargeable zinc-ion batteries. Chin. Chem. Lett. *33*, 1236–1244.
14. Han, M., Huang, J., Liang, S., Shan, L., Xie, X., Yi, Z., Wang, Y., Guo, S., and Zhou, J. (2020). Oxygen defects in β-MnO_2 enabling high-performance rechargeable aqueous zinc/manganese dioxide battery. iScience *23*, 100797.
15. Li, Y., Zhao, J., Hu, Q., Hao, T., Cao, H., Huang, X., Liu, Y., Zhang, Y., Lin, D., Tang, Y., and Cai, Y. (2022). Prussian blue analogs cathodes for aqueous zinc ion batteries. Mater. Today Energy *29*, 101095.
16. Zhang, J., and Wu, X. (2024). Dual-ion carrier storage through Mg^{2+} zinc-ion hybrid capacitor. Int. J. Miner. Metall. Mater. *31*, 179–185.
17. Guan, J., Shao, L., Yu, L., Wang, S., Shi, X., Cai, J., and Sun, Z. (2022). Two-dimensional $Mg_{0.2}V_2O_5 \cdot nH_2O$ nanobelts derived from V_4C_3 MXenes for highly stable aqueous zinc ion batteries. Chem. Eng. J. *443*, 136502.
18. Liu, Y., Liu, Y., Wu, X., and Cho, Y.R. (2022). High performance aqueous zinc battery enabled by potassium ion stabilization. J. Colloid Interface Sci. *628*, 33–40.
19. Tan, X., Zhang, F., Chen, D., Wang, P., Liu, Y., Meng, C., and Zhang, Y. (2024). Modulating NH_4^+ in vanadium oxide framework for high-efficient aqueous NH_4^+ storage. Chem. Eng. J. *489*, 151119.
20. Zhao, C., Liu, Y., Wu, X., and Luo, S. (2024). Graphene oxide wrapped VO_2 nanobelts for calendar-life zn storage devices. Adv. Sustain. Syst. *8*, 2400077.
21. Tan, X., Zhang, F., Chen, D., Gong, J., Sun, J., Meng, C., and Zhang, Y. (2024). One-step hydrothermal synthesis of vanadium dioxide/carbon core-shell composite with improved ammonium ion storage for aqueous ammonium-ion battery. J. Colloid Interface Sci. *669*, 2–13.
22. Zhao, M., Li, S., Wu, X., and Abdukader, A. (2024). The introduction of gallium ions into V_2O_5 interlayers for highly reversible Zn ion batter. Mater. Adv. *5*, 3965–3972.
23. Ye, J.J., Li, P.H., Zhang, H.R., Song, Z.Y., Fan, T.j., Zhang, W.Q., Tian, J., Huang, T., Qian, Y.T., Hou, Z.G., et al. (2023). Manipulating oxygen vacancies to spur ion kinetics in V_2O_5 structures for superior aqueous zinc-ion batterie. Adv. Funct. Mater. *33*, 2305659.
24. Liu, Y., Liu, Y., and Wu, X. (2023). Defect engineering of vanadium-based electrode materials for zinc ion battery. Chin. Chem. Lett. *34*, 107839.
25. Chen, L., Zheng, Y., Zhang, Z., Ma, Y., Wang, Y., Xiao, H., Xu, M., Li, Z., and Yuan, G. (2024). Optimizing ammonium vanadate crystal structure by facile in situ phase

transformation of VO_2/$NH_4V_4O_{10}$ with special micro-nano feature for advanced aqueous zinc ion batteries. Inorg. Chem. Front. *11*, 1266–1278.

26. Zhang, Y., Tao, L., Xie, C., Wang, D., Zou, Y., Chen, R., Wang, Y., Jia, C., and Wang, S. (2020). Defect engineering on electrode materials for rechargeable batteries. Adv. Mater. *32*, 1905923.
27. Guo, C., Yi, S., Si, R., Xi, B., An, X., Liu, J., Li, J., and Xiong, S. (2022). Advances on defect engineering of vanadium-based compounds for high-energy aqueous zinc-ion batteries. Adv. Energy Mater. *12*, 2202039.
28. Zhang, X., Wei, H., Ren, B., Jiang, J., Qu, G., Yang, J., Chen, G., Li, H., Zhi, C., and Liu, Z. (2023). Unlocking high-performance ammonium-ion batteries: activation ofin-layer channels for enhanced ion storage and migration. Adv. Mater. *35*, 2304209.
29. Cao, J., Zhang, D., Yue, Y., Wang, X., Pakornchote, T., Bovornratanaraks, T., Zhang, X., Wu, Z.S., and Qin, J. (2021). Oxygen defect enriched $(NH_4)_2V_{10}O_{25}\cdot 8H_2O$ nanosheets for superior aqueous zinc-ion batteries. Nano Energy *84*, 84105876.
30. Cui, F., Wang, D., Hu, F., Yu, X., Guan, C., Song, G., Xu, F., and Zhu, K. (2022). Deficiency and surface engineering boosting electronic and ionic kinetics in $NH_4V_4O_{10}$ for high-performance aqueous zinc-ion battery. Energy Storage Mater. *44*, 197–205.
31. Du, M., Miao, Z., Li, H., Zhang, F., Sang, Y., Wei, L., Liu, H., and Wang, S. (2021). Oxygen-vacancy and phosphate coordination triggered strain engineering of vanadium oxide for high-performance aqueous zinc ion storage. Nano Energy *89*, 106477.
32. Qi, J., Zhang, Y., Li, M., Xu, H., Zhang, Y., Wen, J., Zhai, H., Yang, W., Li, C., Wang, H., et al. (2023). Facile and effective defect engineering strategy boosting ammonium vanadate nanoribbon for high performance aqueous zinc-ion batteries. J. Colloid Interface Sci. *642*, 430–438.
33. Zhang, N., Dong, Y., Jia, M., Bian, X., Wang, Y., Qiu, M., Xu, J., Liu, Y., Jiao, L., and Cheng, F. (2018). F.Y. Rechargeable aqueous Zn-V_2O_5 battery with high energy density and long cycle life. ACS Energy Lett. *3*, 1366–1372.
34. Wang, Y., Zhang, Y., Gao, G., Fan, Y., Wang, R., Feng, J., Yang, L., Meng, A., Zhao, J., and Li, Z. (2023). Effectively modulating oxygen vacancies in flower-like δ-MnO_2 nanostructures for large capacity and high-rate zinc-ion storage. Nano-Micro Lett. *15*, 219.
35. Zhuang, L., Ge, L., Yang, Y., Li, M., Jia, Y., Yao, X., and Zhu, Z. (2017). Ultrathin iron-cobalt oxide nanosheets with abundant oxygen vacancies for the oxygen evolution reaction. Adv. Mater. *29*, 1606793.
36. Li, S., Xu, X., Chen, W., Zhao, J., Wang, K., Shen, J., Chen, X., Lu, X., Jiao, X., Liu, Y., and Bai, Y. (2024). Synergetic impact of oxygen and vanadium defects endows $NH_4V_4O_{10}$ cathode with superior performances for aqueous zinc-ion battery. Energy Storage Mater. *65*, 103108.
37. Zhang, Y., Du, Y., Song, B., Wang, Z., Wang, X., Wan, F., and Ma, X. (2022). Manganese-ions and polyaniline co-intercalation into vanadium oxide for stable zinc-ion batteries. J. Power Sources *545*, 231920.
38. Feng, Z., Zhang, Y., Sun, J., Liu, Y., Jiang, H., Cui, M., Hu, T., and Meng, C. (2022). Dual ions enable vanadium oxide hydration with superior Zn^{2+} storage for aqueous zinc-ion batteries. Chem. Eng. J. *433*, 133795.
39. Jiang, H., Zhang, Y., Pan, Z., Xu, L., Zheng, J., Gao, Z., Hu, T., and Meng, C. (2020). Facile hydrothermal synthesis and electrochemical properties of $(NH_4)_2V_{10}O_{25}\cdot 8H_2O$ nanobelts for high-performance aqueous zinc ion batteries. Electrochim. Acta *332*, 135506.
40. Jiang, H., Zhang, Y., Xu, L., Gao, Z., Zheng, J., Wang, Q., Meng, C., and Wang, J. (2020). Fabrication of $(NH_4)_2V_3O_8$ nanoparticles encapsulated in amorphous carbon for high capacity electrodes in aqueous zinc ion batteries. Chem. Eng. J. *382*, 122844.
41. Huang, C., Liu, S., Feng, J., Wang, Y., Fan, Q., Kuang, Q., Dong, Y., and Zhao, Y. (2021). Optimizing engineering of rechargeable aqueous zinc ion batteries to enhance the zinc ions storage properties of cathode material. J. Power Sources *490*, 229528.
42. Chen, S., Zhang, Y., Geng, H., Yang, Y., Rui, X., and Li, C.C. (2019). Zinc ions pillared vanadate cathodes by chemical pre-intercalation towards long cycling life and low-temperature zinc ion batteries. J. Power Sources *441*, 227192.
43. Zhang, Y., Jiang, H., Xu, L., Gao, Z., and Meng, C. (2019). Ammonium vanadium oxide $[(NH_4)_2V_4O_9]$ Sheets for high capacity electrodes in aqueous zinc ion batteries. ACS Appl. Energy Mater. *2*, 7861–7869.
44. Zhao, M., Li, S., Umar, A., and Wu, X. (2023). $(NH_4)_2V_{10}O_{25}\cdot 8H_2O$ nanowire materials for stable zinc ion storage. Mater. Today Chem. *33*, 101686.
45. Xu, Y., Fan, G., Sun, P.X., Guo, Y., Wang, Y., Gu, X., Wu, L., and Yu, L. (2023). Carbon nitride pillared vanadate via chemical pre-intercalation towards high-performance aqueous zinc-ion batteries. Angew. Chem. Int. Ed. *62*, e202303529.
46. Zhao, M., Li, S., Wu, X., and Luo, S. (2024). Gallium ion pre-insertion protocol to $(NH_4)_2V_{10}O25\cdot 8H_2O$ cathode materials for reversible aqueous Zn battery. Adv. Mater. Technol. *1*, 2400125.
47. Luo, P., Yu, G., Zhang, W., Tang, H., Zhu, D., Chao, F., Zhong, W., Dong, S., and An, Q. (2024). Triple-synergistic effect" of K^+ and PANI co-intercalation enabling the high-rate capability and stability of V_2O_5 for aqueous zinc-ion batteries. J. Colloid Interface Sci. *659*, 267–275.
48. Xu, W., Sun, C., Wang, N., Liao, X., Zhao, K., Yao, G., Sun, Q., Cheng, H., Wang, Y., and Lu, X. (2021). Sn stabilized pyrovanadate structure rearrangement for zinc ion battery. Nano Energy *81*, 105584.
49. Ding, J., Du, Z., Gu, L., Li, B., Wang, L., Wang, S., Gong, Y., and Yang, S. (2018). Ultrafast Zn^{2+} intercalation and deintercalation in vanadium dioxide. Adv. Mater. *30*, 1800762.
50. Wan, F., Zhang, L., Dai, X., Wang, X., Niu, Z., and Chen, J. (2018). Aqueous rechargeable zinc/sodium vanadate batteries with enhanced performance from simultaneous insertion of dual carriers. Nat. Commun. *9*, 1656.

STAR★METHODS

KEY RESOURCES TABLE

REAGENT or RESOURCE	SOURCE	IDENTIFIER
Chemicals		
NH_4VO_3 powder	Aladdin, 99%	N/A
$H_2C_2O_4 \cdot 2H_2O$	Damao, 99.5%	N/A

EXPERIMENTAL MODEL AND STUDY PARTICIPANT DETAILS

There are no experimental models (animals, human subjects, plants, microbe strains, cell lines, primary cell cultures) used in the study.

METHOD DETAILS

Preparation of $NH_4V_4O_{10}$ nanosheets

All the chemicals were used without further purification. Typically, 4 mmol of NH_4VO_3 powder (Aladdin, 99%) was dissolved into 50 mL of deionized water at 60°C to form light-yellow solution. After cooling to room temperature, 4 mmol of $H_2C_2O_4 \cdot 2H_2O$ (Damao, 99.5%) was added into the above solution and stirred for 0.5 h and transferred into 80 mL Teflon-lined autoclave at 180°C for 3 h. Finally, the samples were washed alternately with alcohol and deionized water and then dried under vacuum for 12 h. The precursors were immersed into 100 mL of 1M $NaBH_4$ solution. In comparison, we synthesized four kinds of samples with different immersion time of 0, 30, 40 and 50 min, respectively. The prepared samples were denoted as NHVO, NHVO-30, NHVO-40 and NHVO-50 in sequence.

Structural characterization

The crystallographic information of the as-obtained samples was studied by X-ray diffraction (XRD, Shimadzu-7000, Cu Kα radiation, λ = 0.1541 nm) and X-ray photoelectron spectrometer (XPS, Thermo Scientific). Scanning electron microscope (SEM, Gemini 300-71-31) and transmission electron microscope (TEM, JEM-2100 PLUS) were utilized to characterize the morphology and microstructure of the material. The vacancies of the materials were verified by electron paramagnetic resonance (EPR) spectroscope (Bruker EMXplue-6/1).

Electrochemical characterization

The CR2032 cells were constructed utilizing the cathodes, glass fiber, 3 M $Zn(CF_3SO_3)_2$ electrolyte (Macklin, 98%) and zinc foil under ambient conditions. The positive electrode consists of the synthetic sample, carbon black (super P, Power Origin Limited) and polyvinylidene fluoride (PVDF, Power Origin Limited) with the ratio of 7:2:1. N-methyl-*l*-2-pyrrolidone (NMP, Damao, 99%) is then added to the mixed powder to form a slurry, which was coated on a carbon paper. A Neware battery tester (CT-4008T-5V6A-164) was used to evaluate the cycling stability and rate performance. Finally, the electrochemical impedance spectra (EIS) and cyclic voltammetry (CV) curves were performed in a CHI660E electrochemical workstation.

QUANTIFICATION AND STATISTICAL ANALYSIS

This study does not include statistical analysis or quantification.

ADDITIONAL RESOURCES

This work does not include any additional resource.